iScience

Article

Ga@MXene-based flexible wearable biosensor for glucose monitoring in sweat

Graphical abstract

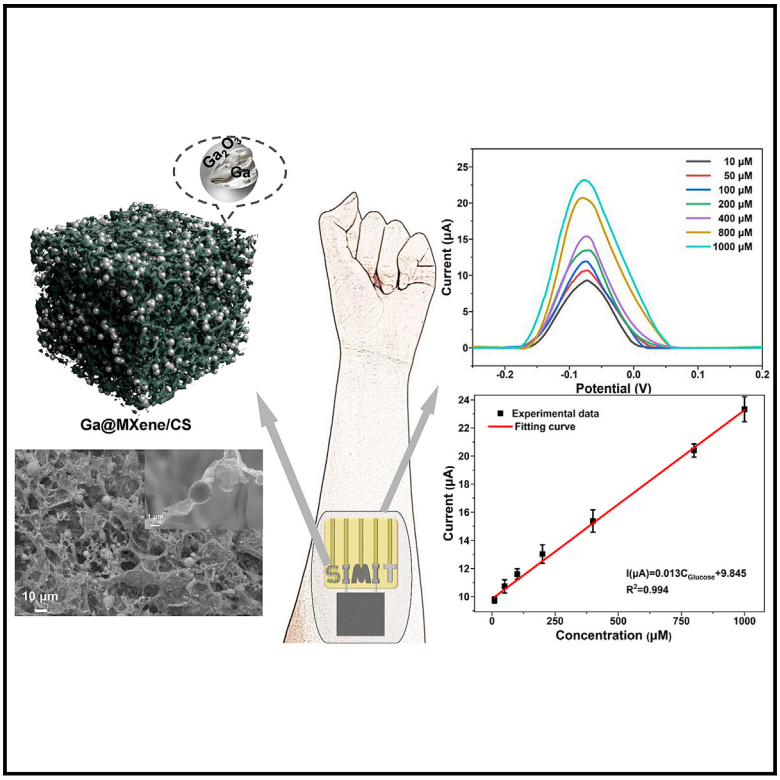

Highlights

- The electrochemical glucose detection was performed on the Ga@MXene/CS-based wearable sensor
- The sensor features a conductive, three-dimensional porous structure based on Ga@MXene
- The sensor has a linear range of 10–1,000 μM, a limit of detection as low as 0.77 μM
- In real sample testing, the recovery rate of the sensor ranged from 95.5% to 107.1%

Authors

Wensi Zhang, Shuyue Jiang, Hongquan Yu, Shilun Feng, Kaihuan Zhang

Correspondence

shilun.feng@mail.sim.ac.cn (S.F.), kzhang@mail.sim.ac.cn (K.Z.)

In brief

Health sciences; Natural sciences; Applied sciences

Zhang et al., 2025, iScience *28*, 111737
February 21, 2025
https://doi.org/10.1016/j.isci.2024.111737

CellPress

iScience

CellPress
OPEN ACCESS

Article

Ga@MXene-based flexible wearable biosensor for glucose monitoring in sweat

Wensi Zhang,[1,2,4] Shuyue Jiang,[1,2,4] Hongquan Yu,[1,2,3] Shilun Feng,[1,3,*] and Kaihuan Zhang[1,2,3,5,*]

[1]State Key Laboratory of Transducer Technology, Shanghai Institute of Microsystem and Information Technology, Chinese Academy of Sciences, Shanghai 200050, China

[2]2020 X-Lab, Shanghai Institute of Microsystem and Information Technology, Chinese Academy of Sciences, Shanghai 200050, China

[3]School of Graduate Study, University of Chinese Academy of Sciences, Beijing 100049, China

[4]These authors contributed equally

[5]Lead contact

*Correspondence: shilun.feng@mail.sim.ac.cn (S.F.), kzhang@mail.sim.ac.cn (K.Z.)

https://doi.org/10.1016/j.isci.2024.111737

SUMMARY

Most wearable biosensors struggle to balance flexibility and conductivity in their sensing interfaces. In this study, we propose a wearable sensor featuring a highly stretchable, three-dimensional conductive network structure based on liquid metal. The sensor interface utilizes a patterned Ga@MXene hydrogel system, where gallium (Ga) grafted onto MXene provides enhanced electrical conductivity and malleability. MXene provides excellent conductivity and a three-dimensional layered structure. Additionally, the chitosan (CS) hydrogel, with its superior water absorption and stretchability, allows the electrode to retain sweat and closely stick to the skin. The sensor demonstrates a low limit of detection (0.77 μM), high sensitivity (1.122 $\mu A \cdot \mu M^{-1} \cdot cm^{-2}$), and a broad detection range (10–1,000 μM), meeting the requirements for a wide range of applications. Notably, the sensor can also induce perspiration in the wearer. The three-dimensional porous structure of the Ga@MXene/CS biosensor ensures excellent conductivity and flexibility, making it suitable for a variety of applications.

INTRODUCTION

The increasing focus on personal health and the urgent need for rapid biochemical information in non-clinical settings are driving advancements in novel monitoring technologies.[1] Wearable electrochemical sensors, characterized by their miniaturization, portability, and real-time monitoring capabilities, are now in high demand.[1] Sweat has emerged as a preferred medium for testing and sampling due to its easy accessibility and non-invasive nature compared to blood.[2,3] The chemical composition of sweat, which includes biomarkers such as glucose, lactate, cortisol, dopamine, potassium, and sodium, is a key driver in the development of wearable sensors.[4–7] Monitoring blood glucose levels is particularly crucial for preventing conditions such as hypoglycemia and diabetes, highlighting the importance of real-time analysis.[8] Given the evident correlation between glucose levels in sweat and blood, the glucose content in sweat is only 1%–2% of that found in blood (10–1,000 μM).[9,10] Consequently, traditional hospital blood glucose testing equipment is not suitable for detecting glucose levels in sweat. Therefore, researchers are increasingly focusing on the development of wearable sensors for non-invasive glucose analysis. Tang et al. introduced a wearable biosensor based on carbon black nanoparticles for detecting glucose in human sweat.[11] Hekmat et al. engineered commercial cotton fabrics decorated with binary Ni-Co metal-organic frameworks for non-enzymatic amperometric glucose sensing.[12] Zhang et al. developed copper-silver bimetallic oxide nanowires on Cu-Ag electrodes for glucose detection.[13] As these studies have shown, most wearable sensors rely on the design of traditional electrochemical sensors. Although research on wearable devices has provided an increasing number of highly stretchable structures, their construction still involves embedding rigid materials with high conductivity into the elastic structure to achieve their detection functions.[14] The limited ductility of these conductive materials in the working electrode poses challenges when integrating the sensor with the skin. Poor ductility can lead to interface breakage or increased resistance when the electrodes are bent or stretched, ultimately reducing sensor sensitivity.

Gallium (Ga) is a liquid metal with a low melting point, characterized by high malleability, elevated surface tension, and excellent electrical conductivity.[15] Additionally, Ga possesses excellent imaging properties. Zhu et al.[16] developed a type of drug-loaded microsphere with liquid metal, which can be injected to embolize blood vessels in rabbit ears. The introduction of liquid metal particles enables the microspheres to be imaged under various imaging equipment for multimodal imaging. Gao et al.[17] utilized the linear thermal expansion property of Ga to create a new type of nanoscale thermometer. In this study, Ga was filled into carbon nanotubes to form a Ga metal column that expands highly linearly with temperature changes. The measurement range of this nano thermometer can be extended to 50°C to 500°C, and it has high sensitivity and accuracy. Owing to the high deformability of Ga, it can seamlessly conform to

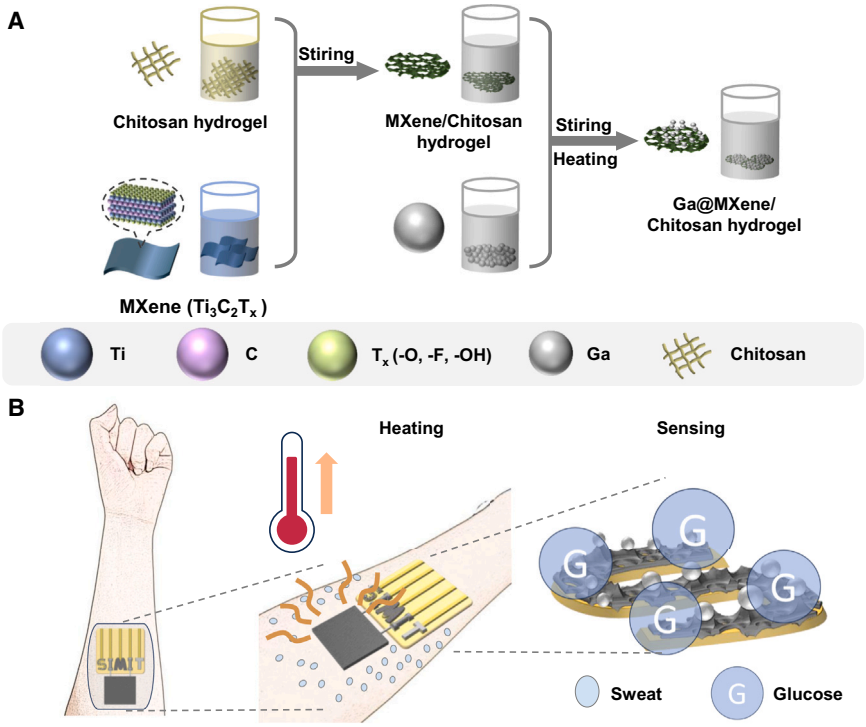

Figure 1. Preparation diagram and detection schematic of wearable sensors

(A) Preparation diagram of Ga@MXene/CS.

(B) Detection principle schematic diagram of Ga@MXene/CS sensor.

the skin's surface and maintain constant conductivity during stretching. Therefore, its application prospects in wearable sensors are very broad.[18] However, its high surface tension and low viscosity cause Ga particles to readily coalesce to minimize surface energy, leading to uneven distribution and posing challenges for uniform application.[19]

MXene is a two-dimensional material known for its excellent mechanical properties, metal-like conductivity, hydrophilicity, tunable interlayer spacing, and electrochemically active surface. These attributes make MXene highly suitable for sensor applications.[20–22] However, van der Waals forces between the layers often result in aggregation and layer overlap, which can hinder performance. To address this issue, metal adsorption onto the MXene surface via electrostatic interactions increases interlayer spacing and connects the monolayers, forming a three-dimensional structure. This strategy mitigates aggregation and enhances the mechanical and electrochemical properties of MXene, offering improved functionality in sensor applications.[23] Wang et al.[24] developed a self-healing strain sensor based on $Ti_3C_2T_x$ MXene/AgNW/liquid metal, where Ga primarily serves as a connector and bridge, enhancing the interfacial interaction between MXene and AgNW. This compensates for some of the shortcomings of MXene in self-healing strain sensors, improving the stability and mechanical properties of the sensor.

In this study, we developed a wearable sensor using a combination of Ga, MXene, and chitosan hydrogels, as shown in Figure 1. The synergistic interaction between Ga and MXene resulted in the formation of a porous structure with both high conductivity and deformability. The incorporation of Ga into the MXene/chitosan hydrogel (MXene/CS) led to the grafting of Ga onto MXene. The resulting Ga@MXene/chitosan hydrogel (Ga@MXene/CS) exhibited increased interlayer spacing, as Ga particles penetrated the MXene/CS structure. These liquid metal particles supported and interconnected the porous network, thereby enhancing electrical conductivity. Additionally, the MXene/CS matrix anchored the Ga particles through grafting, ensuring uniform dispersion. This structure was employed to fabricate a self-sweat-generating electrochemical wearable sensor for *in situ* glucose detection in sweat (Figure 1). The structural and chemical properties of Ga@MXene/CS were characterized using scanning electron microscopy (SEM), X-ray diffraction (XRD), and X-ray photoelectron spectroscopy (XPS). The electrochemical performance was evaluated through cyclic voltammetry (CV) and electrochemical impedance spectroscopy (EIS). Glucose detection in human sweat was conducted using differential pulse voltammetry (DPV).

RESULTS AND DISCUSSION

Characterization of Ga@MXene/CS

The morphology and elemental distribution images of Ga@MXene/CS were investigated through SEM and energy-dispersive spectroscopy (EDS). Figure 2 presents the SEM images and energy spectrum analysis of Ga@MXene/CS. In Figures 2A and 2B, Ga@MXene/CS exhibits a continuous porous structure with pore sizes ranging from approximately 5 to 15 μm. In comparison, the SEM image of MXene/CS (Figure S1) reveals an irregular layered structure characterized by numerous folds. Compared with the layered structure of MXene/CS, the three-dimensional porous structure of Ga@MXene/CS provides a larger surface area for the working electrode, enhancing the capacity of the sensor to absorb and detect glucose molecules in sweat. Figure 2C explains why Ga@MXene/CS exhibits a three-dimensional porous structure. In this structure, Ga particles are embedded between the MXene monolayers, connecting and organizing them into a three-dimensional porous network. This transformation from a two-dimensional to an ordered three-dimensional structure increases the available surface area for electrochemical reactions. Figure 1 outlines the preparation principle of Ga@MXene/CS, highlighting that the abundance of surface functional groups in MXene provides multiple hydrogen bonding sites that facilitate cross-linking with CS hydrogels, while the network structure of CS is effective in preventing MXene monolayer stacking.[25–27]

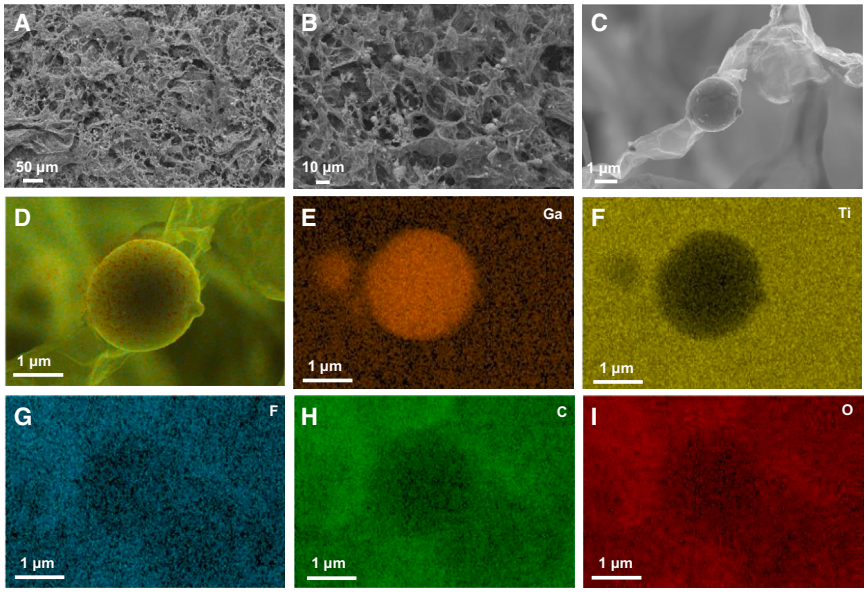

Figure 2. Morphology and elemental distribution images of Ga@MXene/CS

(A–C) SEM images of Ga@MXene/CS. Scale bar: 50, 10, and 1 μm in order.

(D–I) EDS images of Ga@MXene/CS. Scale bar: 1 μm.

Furthermore, the incorporation of Ga, embedded between the MXene monolayers, establishes bonding interactions with MXene, contributing to the formation of a stable structure.[28] The porous architecture of Ga@MXene/CS also minimizes the aggregation tendency of Ga particles.[29] As shown in Figures 2D–2I, EDS analysis reveals that elements such as Ti, F, and C from MXene are uniformly distributed on the Ga spheres due to the interaction between MXene and Ga. Additionally, there is evidence of minor Ga penetration into the MXene structure, further contributing to the uniform distribution and stability of the composite.

To investigate the interaction between Ga and MXene in Ga@MXene/CS, a comparative analysis of the XRD patterns for Ga/CS, MXene/CS, and Ga@MXene/CS was conducted (Figures 3A and 3B). In Figure 3A, the XRD pattern for Ga/CS shows peaks corresponding to the (002), (111), (112), (200), (113), (211), and (220) planes of Ga (JCPDS No. 05-0601). In the XRD pattern for MXene/CS ($Ti_3C_2T_x$/CS), the diffraction peaks at (002), (004), (006), (101), (105), (108), (109), and (110) are attributed to the planar diffraction of $Ti_3C_2T_x$.[30,31] The sharp diffraction peaks in the XRD pattern of Ga@MXene/CS, corresponding to those of Ga/CS and MXene/CS, confirm the presence of both Ga and MXene within the Ga@MXene/CS composite. Additionally, as shown in Figure 3B, the diffraction peaks in Ga@MXene/CS exhibit shifts to specific angles. Notably, the (111) and (200) diffraction peaks of Ga in Ga@MXene/CS shift to higher angles (from 30.3° to 30.4° and from 39.84° to 39.98° 2θ, respectively). According to Bragg's law, this shift indicates a contraction in the Ga lattice. The contraction is attributed to the bonding of Ti^{4+} ions with Ga, as the atomic radius of Ti (140 pm) is smaller than that of Ga (187 pm), leading to lattice contraction upon Ti^{4+} doping. In contrast, the (006) and (101) diffraction peaks of MXene in Ga@MXene/CS shift to lower angles (from 21.66° to 21.51° and from 34.49° to 33.8° 2θ, respectively). These shifts result from the increased interlayer spacing in MXene due to the incorporation of Ga particles within the MXene/CS structure.[32]

To further investigate the chemical bonds formed by the interaction between MXene and Ga in Ga@MXene/CS, the X-ray photoelectron spectra of Ga/CS, MXene/CS, and Ga@MXene/CS are presented in Figures 3C–3F. In Figure 3C, the primary elements detected in Ga@MXene/CS are Ga, Ti, C, and O. The Ga and Ti peaks correspond to those observed in Ga/CS and MXene/CS, respectively. The XPS data for Ga@MXene/CS are consistent with the results obtained from XRD and EDS analyses. Figure 3D provides a detailed examination of the Ga element. In Ga/CS, the Ga peak is detected at 17.68 eV, with an additional peak for Ga_2O at 18.92 eV and the more stable oxide, Ga_2O_3, at 20.21 eV, resulting from the oxidation of the Ga surface. The presence of these oxide peaks indicates that the Ga surface is prone to oxidation, leading to the formation of Ga_2O_3, a more stable form.[33] When two oxides with different valence states coexist, the presence of Ga^+ in the lower valence state can generate additional oxygen vacancies in Ga/CS. These oxygen vacancies introduce defects with positive ions within the crystal structure, which can enhance the conductivity of the material.[34] In Ga@MXene/CS, the XPS spectrum reveals three distinct peaks corresponding to Ga–O (17.68 eV), Ga–O–Ti (19.68 eV), and Ga_2O_3 (20.22 eV). The disappearance of the Ga_2O peak and the appearance of the Ga–O–Ti peak suggest that, following the cleavage of the Ga–O bond, Ti from MXene reacts with Ga to form the Ga–O–Ti bond. This indicates that the doping of MXene influences the formation of new chemical bonds involving Ga and Ti.[35] The XPS peaks shown in Figure 3E can be deconvoluted into three pairs of Ti 2p doublets: Ti–O (461.98/455.68 eV), Ti–O_x (463.88/458.18 eV), and Ti–C (460.38/454.38 eV). These doublets correspond to the oxygen-terminated state of Ti_3C_2, the oxidation states of Ti_3C_2, and the Ti–C bonds within Ti_3C_2, respectively.[25,36] In Ga@MXene/CS, the Ti–O bonds previously observed at 461.98 and 455.68 eV disappear, indicating that these Ti–O bonds have been transformed into other components. Figure 3F displays the O 1s spectra for the three modified layers. In the Ga/CS spectrum, three peaks were deconvoluted: Ga–O at 529.48 eV, oxygen vacancies at 531.48 eV, and C–OH at 533.76 eV, the latter originating from CS.[25] In the MXene/CS spectrum, four peaks were identified: Ti–O at 528.88 eV, C–Ti–O_x at 530.35 eV, C–Ti–OH_x at 532.18 eV, and C–OH at 533.78 eV.[37] In the Ga@MXene/CS spectrum, five peaks were identified: Ti–O at 528.88 eV, Ga–O at 529.50 eV, Ga–O–Ti at 531.17 eV,

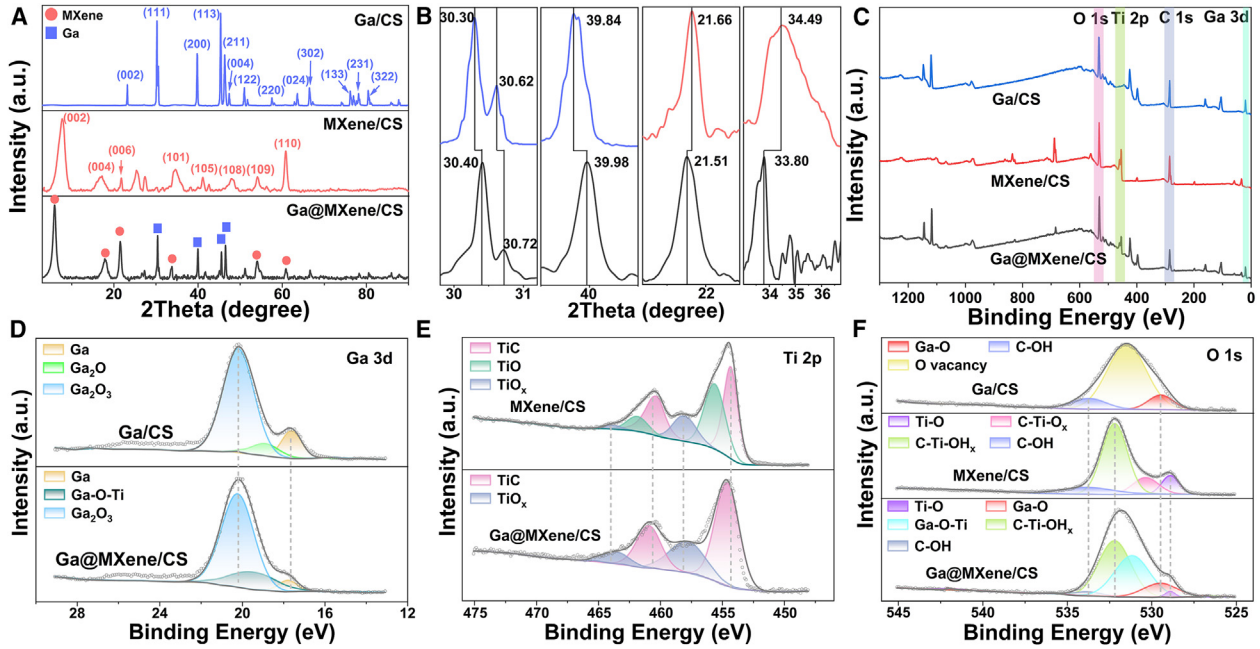

Figure 3. Characterization of structure and composition of materials

(A and B) XRD patterns for Ga/CS, MXene/CS, and Ga@MXene/CS.

(C) XPS survey spectra of Ga/CS, MXene/CS, and Ga@MXene/CS.

(D–F) Ga 3d spectrum, Ti 2p spectrum, and O 1s spectrum of Ga/CS, MXene/CS, and Ga@MXene/CS.

C–Ti–OH_x at 532.22 eV, and C–OH at 533.78 eV. The presence of the Ga–O–Ti peak and the observed shifts in the XRD results (Figure 3B) confirm the successful grafting of Ga onto MXene. Additionally, the formation of Ga–O–Ti bonds also prevents the Ga spheres from detaching from the modification layer, affecting the detection performance of the sensor. Moreover, the network structure of CS in the SEM image and the C–OH bond of XPS proved that CS hydrogel with good adhesion is the first choice for constructing the sensor.

Electrochemical properties of the wearable electrodes

To evaluate the electrochemical properties and redox capabilities of three flexible electrodes—Ga/CS, MXene/CS, and Ga@MXene/CS—CV and electrochemical impedance spectroscopy techniques were employed. The electrodes were tested using a 300 μM glucose solution prepared with 0.01 M PBS buffer. Figures 4A–4C display the CV results for the three electrodes. The oxidation current peak of Ga@MXene/CS is significantly higher compared to MXene/CS and Ga/CS at the same scan rate, indicating superior redox capabilities of the Ga@MXene/CS electrode. This enhancement is attributed to the high surface area provided by the three-dimensional porous structure, which offers more reaction sites for glucose, and the high electrical conductivity of Ga, which facilitates rapid glucose oxidation. Additionally, to investigate the electrochemical kinetics, CV tests were performed at varying scan rates (30–110 mV/s). The current responses of all three electrodes increased progressively with increasing scan rates, suggesting that the redox processes of the modified electrodes are quasi-reversible. Figure 4D presents the regression equations for the anodic and cathodic peak currents of the electrodes. The electroactive surface areas of the electrodes were comparatively analyzed using the Randles-Sevcik equation.[38]

$$I_p = 2.69 \times 10^5 A D^{\frac{1}{2}} n^{\frac{3}{2}} v^{\frac{1}{2}} C$$

where I_P, n, A, υ, D, and C indicate peak current (A), number of electron transfers in the redox event, effective surface area (cm^2), scan rate (V/s), diffusion coefficient (cm^2/s), and bulk concentration of analyte (mol/L), respectively. Since the test solution is 100 μM glucose, D, n, and C are constants. Thus, the peak current is positively related only to the scanning speed, while the electroactive surface area will be proportional to the Randles-Sevcik equation. In Figure 4D, the slopes of the oxidation reactions are $2.426E^{-5}$ (Ga@MXene/CS), $1.283E^{-5}$ (MXene/CS), and $1.336E^{-5}$ (Ga/CS), respectively. By comparison, Ga@MXene/CS has the largest electroactive surface area. Therefore, the excellent performance of the mesh structure of grafted Ga is demonstrated.

The EIS test provides detailed information on the electron transfer behavior of the electrode surface. Figure 4E displays the Nyquist plots for the three flexible electrodes. Figure 4F shows the equivalent circuit diagram used to model the electrochemical reaction process. R_s represents the internal resistance of the detection solution, CPE is the bilayer capacitance so that no chemically reactive ions occur in the solution, R_{ct} represents the charge transfer resistance for the charge transfer process, and W_o is the Warburg impedance for the diffusion process.[39]

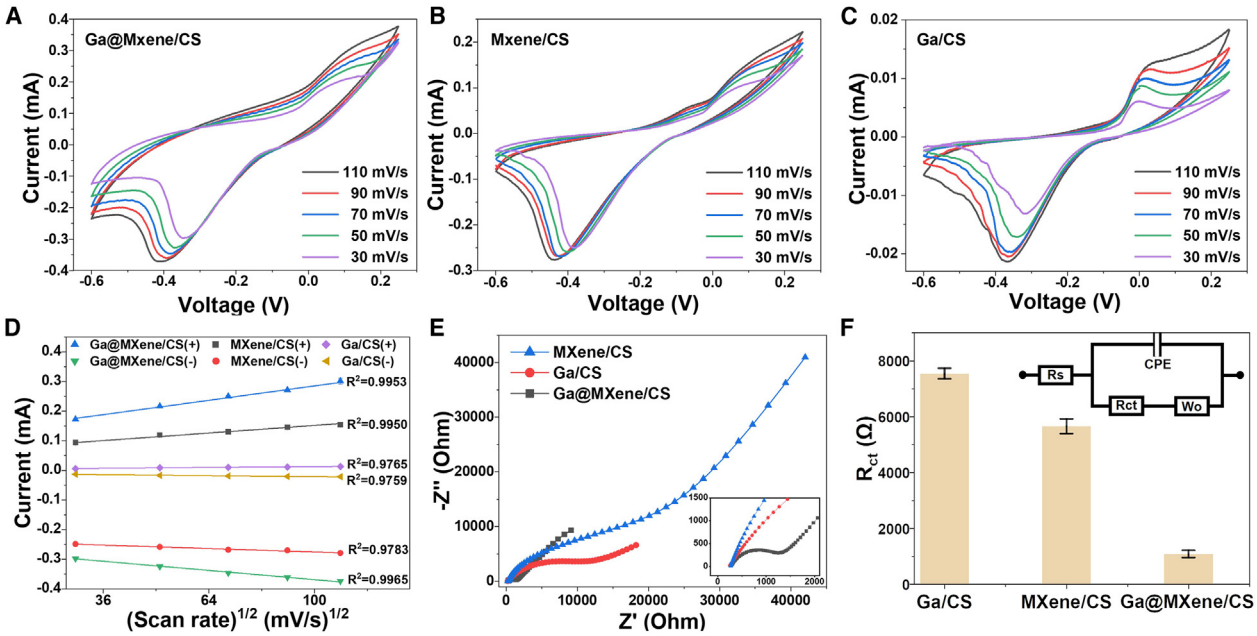

Figure 4. Electrochemical characterization of the wearable sensor

(A–C) CV curves of (A) Ga@MXene/CS, (B) MXene/CS, and (C) Ga/CS at different scan rates.

(D) The calibration of peak currents vs. the root-squared scan rate.

(E) EIS of the Ga/CS, MXene/CS, and Ga@MXene/CS.

(F) Equivalent circuit and charge transfer resistance of the Ga/CS, MXene/CS, and Ga@MXene/CS. Data represented as mean ± standard error of the mean.

In Figure 4E, the R_{ct} values are 7,456 Ω for Ga/CS, 5,762 Ω for MXene/CS, and 1,020 Ω for Ga@MXene/CS. The Ga@MXene/CS electrode exhibits the lowest R_{ct}, indicating superior charge transfer properties compared to the other two electrodes. The improved performance of Ga@MXene/CS can be attributed to the grafting of Ga particles onto MXene, transforming the original two-dimensional structure into a three-dimensional porous network. This structural transformation increases the contact area on the electrode surface, thereby reducing resistance. Compared to Ga/CS, the grafting of Ga onto MXene in Ga@MXene/CS leads to a more uniform dispersion of Ga particles, avoiding aggregation and enhancing conductivity. Additionally, the homogeneous integration of MXene with the hydrogel improves the overall conductivity of the modified layer, creating a continuous conductive pathway. Consequently, the electron transfer rate of the Ga@MXene/CS flexible electrode is significantly enhanced.

Optimization of experimental parameter

Ga spheres in the modification layer not only serve a connective role but also capitalize on their ductility and conductivity, making them a key factor in determining the performance of the sensor. To optimize the performance of the sensor, it is essential to conduct in-depth research on the distribution and particle size of the Ga spheres.

Ga sphere suspensions were fabricated using different ultrasonic powers (240, 320 and 400 W), as depicted in Figure S2. The spheres were primarily sized into two groups: 10–20 μm and less than 1 μm. At 60% power, the production of spheres was scarce (Figures S2A and S2D). At 80% power, there was an increase in sphere quantity and a denser distribution (Figures S2B and S2E). The 100% power treatment (Figures S2C and S2F) yielded the highest sphere count, especially those below 1 μm, enhancing electrical conductivity and the porous structure.

At 100% ultrasonic power, the concentration of the Ga dispersion is maximized, indicating that the distribution of Ga spheres in the modification layer is the densest. To further investigate the influence of ultrasonic power on electrochemical performance, we subjected the three sensors, fabricated using different power levels, to CV tests with a 100 μM glucose solution. The test results are presented in Figure S3. Notably, the sensor constructed with Ga spheres obtained from ultrasonication at 100% power exhibits the largest oxidation peak current value, indicating superior electrochemical performance.

Glucose sensing performance of Ga@MXene/CS wearable biosensor

After evaluating the electrochemical performance, Ga@MXene/CS demonstrated significant advantages. Consequently, the glucose detection performance of Ga@MXene/CS was assessed using DPV. Figure 5A displays the DPV curves for glucose concentrations ranging from 10 to 1,000 μM. The DPV peak current of the modified electrode increased progressively with rising glucose concentrations. The linear regression equation for the sensor is given by:

$$I(\mu A) = 0.013C_{glucose} + 9.845$$

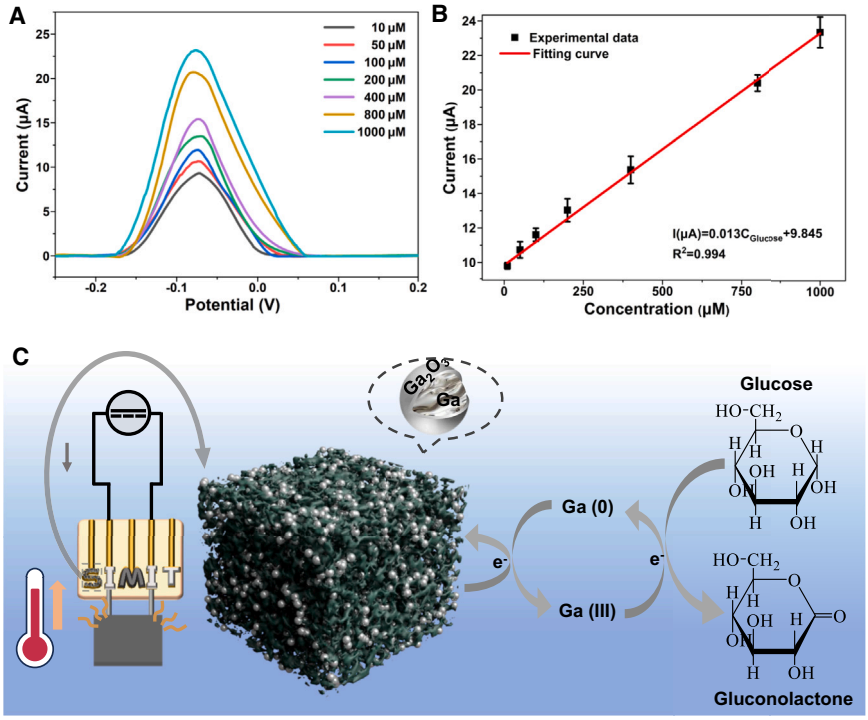

Figure 5. Glucose detection performance and the detection principle diagram

(A) DPV curves of Ga@MXene/CS sensor.

(B) Calibration curve of Ga@MXene/CS biosensor current versus concentration. Data represented as mean ± standard error of the mean.

(C) Ga@MXene/CS sensor detection schematic.

The surface area of the working electrode is 0.01158 cm^2, resulting in a sensitivity of 1.122 $\mu A \cdot \mu M^{-1} \cdot cm^{-2}$. The limit of detection (LOD) can be determined from the equation:[25]

$$LOD = 3s/d$$

where s represents the standard deviation of blank solutions (Figure S4) and d is the slope of the regression equation. Using this information, the LOD for the sensor was calculated to be 0.77 μM. DPV measurements were performed over a glucose concentration range of 10–1,000 μM (Figure 5C), encompassing the glucose concentration ranges relevant to both hypoglycemic and hyperglycemic conditions in sweat.

Figure 5C illustrates the detection schematic of the Ga@MXene/CS wearable sensor. When the electrochemical detection system is immersed in a glucose solution, the surface of Ga particles in the Ga@MXene/CS material is initially covered by a layer of Ga_2O_3.[40] The glucose oxidation process occurs in three stages: (1) glucose molecules are adsorbed onto the electrode surface, (2) with an applied positive potential, Ga(0) is oxidized to Ga(III), releasing electrons, and (3) Ga(III) catalyzes the oxidation of glucose to produce gluconolactone.[41] The redox reaction at the electrode surface can be described by the following equation.

$$Ga \rightarrow Ga^{3+}$$

$$Ga^{3+} + Glucose \rightarrow Ga + Glucolactone$$

Moreover, the three-dimensional porous structure of Ga@MXene/CS increases the electrode surface area, allowing for a greater number of Ga particles to be grafted onto the structure. This increased surface area facilitates the rapid adsorption and reaction of glucose molecules, thereby improving the sensitivity of the sensor.

Table 1 summarizes various wearable sensors with different modified electrodes developed for glucose detection in sweat. A comparative analysis indicates that the Ga@MXene/CS wearable sensor exhibits a notably low LOD of 0.77 μM and a wide detection range of 10–1,000 μM, accommodating the needs of both hypoglycemic and diabetic patients. This performance is attributed to the synergistic effects of Ga@MXene/CS, which leverages the catalytic properties of MXene, the superior water absorption of the hydrogel, and the high conductivity of Ga. The Ga particles contribute to the formation of a cohesive three-dimensional porous structure, enhancing the sensor's overall functionality. Consequently, the Ga@MXene/CS wearable sensor demonstrates broader application potential compared to the sensors listed in Table 1. The LOD, sensitivity, and linear range of the sensors are listed in the table. Compared to the other sensors, the linear range of Ga@MXene/CS is not as wide, but it has a lower LOD as well as higher sensitivity, which enables it to be used for the detection of lower glucose concentrations.

Study of other properties of wearable sensors

To evaluate reproducibility, five Ga@MXene/CS wearable sensors from different batches were tested for peak current values in 0 and 200 μM glucose solutions. As shown in Figure S5A, the peak current differences (ΔI) among the five samples were consistent, ranging from a maximum of 9.32 μA to a minimum of 9.28 μA, with a relative standard deviation of 0.16% (n = 5). This indicates that the reproducibility of the Ga@MXene/CS sensor meets the required standards. For stability assessment, we tested the sensors for peak current differences between 0 and 200 μM glucose solutions at different days after preparation. The sensor showed the highest detection sensitivity on day 0 with a maximum current change (ΔI) of 9.29 μA (Figure S5B). As the number of days increased, the performance of the sensor decreased slightly, with ΔI dropping to 8.68 μA for 15 days, retaining 93.4% of the initial glucose oxidation current. This indicates that the glucose detector maintained good stability. In the selectivity test of the sensor, we selected common substances found in sweat, including NaCl, ascorbic acid, and uric acid, as interfering

Table 1. The comparisons of performance with other reported glucose wearable sensors

Electrodes	Linear range (μM)	LOD (μM)	Sensitivity (μA mM^{-1} cm^{-2})	Reference
$CoWO_4$/CNT/AuNS	0–300	1.3	10.89	Lin et al.[42]
Enzymatic membrane/NiHCF/PB/Au	25–200	10	0.0418	Mirzajani et al.[43]
AuNPs	100–1,000	24	1.27	Li et al.[44]
Glucose oxidase/chitosan/MB/$Ti_3C_2T_x$	80–1,250	17.05	0.0024	Zhang et al.[45]
Ga@MXene/CS	10–1,000	0.77	1122	This work

substances. These interfering substances and glucose were individually diluted with PBS to prepare 600 μM solutions for detection. The results shown in Figure S5C indicate that the wearable sensor did not exhibit significant signal responses to these substances and was not interfered with by other components in sweat. Therefore, the sensor demonstrates good selectivity.

To characterize the thermal response of the sensor, a constant voltage source was connected to the heater of the sensor, and the temperature range was controlled by adjusting the applied voltage. As depicted in Figure 6B, the temperature increased from 23°C to 51°C with rising voltage. Further analysis in Figure 6C shows a nonlinear relationship between $\Delta R/R_0$ and temperature (R^2 = 0.997). To determine the impact of temperature on the heater, the temperature coefficient of resistance (TCR) formula was applied:[45]

$$TCR = \frac{\Delta R}{R_0 \cdot \Delta T}$$

The TCR was determined using the formula, where ΔR represents the resistance change corresponding to the temperature change ΔT and R_0 is the initial resistance value. As shown in Figure 6D, the TCR was 40% at 23°C but decreased rapidly with increasing temperature, leveling off around 25°C. Between 30°C and 50°C, the TCR remained below 1%, indicating that the heater's resistance remains stable within the temperature range relevant to sweat production. This suggests good stability of the heater.

To evaluate the sensor's performance in realistic conditions, glucose sample solutions with concentrations of 25, 75, 300, 500, and 900 μM were prepared using artificial sweat (pH 6.4) and tested. The DPV detection curves in Figure 6E reveal that the peak current increases with glucose concentration. The recovery rates ranged from 95.5% to 107.1% (Figure 6F), demonstrating the high reliability of Ga@MXene/CS sensor for glucose detection in real sweat samples.

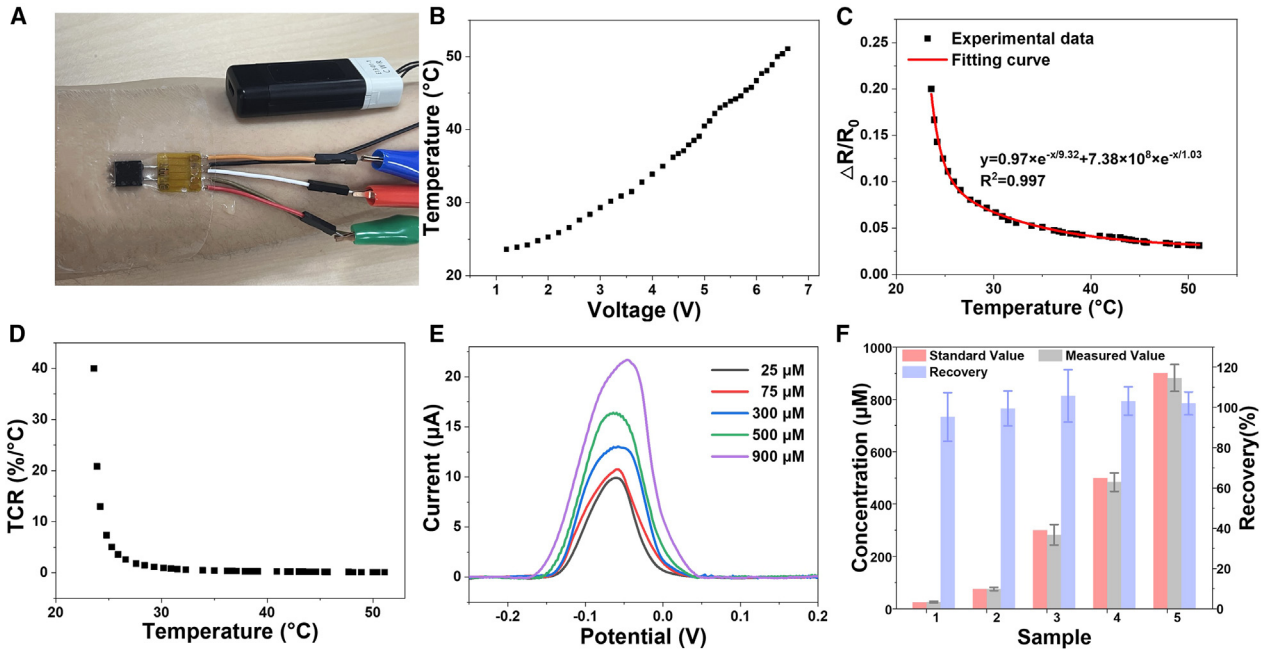

Figure 6. Performance tests of the wearable sensors

(A) Actual image of Ga@MXene/CS sensor.

(B–D) Test chart of the heating function of the Ga@MXene/CS sensor.

(E) DPV curves of Ga@MXene/CS sensors for real sample detection.

(F) Recovery plot of Ga@MXene/CS sensor for real sample detection. Data represented as mean ± standard error of the mean.

Conclusion

In summary, we developed an enzyme-free electrochemical flexible wearable sensor capable of self-heating to induce sweating and *in situ* glucose detection. MXene was crosslinked with CS hydrogel to form MXene/CS, and the addition of Ga led to the formation of Ga–O–Ti bonds through reactions with natural oxides on the surface of Ga, resulting in a Ga@MXene/CS with a three-dimensional porous structure. The sensor leverages the catalytic properties of MXene, the high water absorption of the hydrogel, and the high conductivity of Ga. The Ga particles enhance connectivity within the 3D structure, increasing the electrode's surface area for optimal sweat absorption and glucose binding. This design achieves a low LOD of 0.77 μM and a broad linear range of 10–1,000 μM, with recovery rates between 95.5% and 107.1% in real sample tests. The flexible wearable sensor not only induces sweating through self-heating but also maintains high sensitivity and flexibility, making it suitable for practical skin applications.

Limitations of the study

For wearable biosensors, it is necessary not only to have good detection performance but also to achieve the storage of sweat. The storage of a quantified amount of sweat can make the detection of biochemical substances in sweat more accurate, which is a problem that wearable sensors need to focus on solving in the future.

RESOURCE AVAILABILITY

Lead contact

Further information and requests should be directed to and will be fulfilled by the lead contacts, Kaihuan Zhang (kzhang@mail.sim.ac.cn).

Materials availability

This study did not generate new unique reagents.

Data and code availability

- All data reported in this paper will be shared by the lead contact upon request.
- This paper does not include original code.
- Any additional information required to reanalyze the data reported in this paper is available from the lead contact upon request.

ACKNOWLEDGMENTS

This research was supported by the National Key Research and Development Program of China (grant no. 2021YFF1200800), the National Natural Science Foundation of China (grant no. 62401555), and the Postdoctoral Fellowship Program of CPSF under grant number GZC20232838. Additional support was provided by the Science and Technology Commission of Shanghai Municipality Project (XTCX-KJ-2024-038).

AUTHOR CONTRIBUTIONS

Conceptualization, W.Z. and S.J.; methodology, W.Z. and S.J.; optimization, W.Z., S.J., and H.Y.; writing – original draft, W.Z. and S.J.; supervision, K.Z. and S.F.; funding acquisition, K.Z. and S.F.; writing – review and editing, K.Z. and S.F.

DECLARATION OF INTERESTS

The authors declare no competing interests.

STAR★METHODS

Detailed methods are provided in the online version of this paper and include the following:

- KEY RESOURCES TABLE
- EXPERIMENTAL MODEL AND SUBJECT DETAILS
- METHOD DETAILS
  - Preparation of Ga@MXene/CS sensor
  - Three-electrode system and sweat generator
  - Characterization
- QUANTIFICATION AND STATISTICAL ANALYSIS
- ADDITIONAL RESOURCES

SUPPLEMENTAL INFORMATION

Supplemental information can be found online at https://doi.org/10.1016/j.isci.2024.111737.

Received: August 19, 2024
Revised: September 11, 2024
Accepted: December 31, 2024
Published: January 2, 2025

REFERENCES

1. Bariya, M., Nyein, H.Y.Y., and Javey, A. (2018). Wearable sweat sensors. Nat. Electron. *1*, 160–171. https://doi.org/10.1038/s41928-018-0043-y.
2. Sim, D., Brothers, M.C., Slocik, J.M., Islam, A.E., Maruyama, B., Grigsby, C.C., Naik, R.R., and Kim, S.S. (2022). Biomarkers and detection platforms for human health and performance monitoring: a review. Adv. Sci. *9*, 2104426. https://doi.org/10.1002/advs.202104426.
3. Gao, F., Liu, C., Zhang, L., Liu, T., Wang, Z., Song, Z., Cai, H., Fang, Z., Chen, J., Wang, J., et al. (2023). Wearable and flexible electrochemical sensors for sweat analysis: a review. Microsyst. Nanoeng. *9*, 1–21. https://doi.org/10.1038/s41378-022-00443-6.
4. Ma, X., Wu, X., Luo, W., Liu, Z., Wang, F., and Yu, H. (2024). Large-Scale Wearable Textile-Based Sweat Sensor with High Sensitivity, Rapid Response, and Stable Electrochemical Performance. ACS Appl. Mater. Interfaces *16*, 18202–18212. https://doi.org/10.1021/acsami.4c01521.
5. Zhang, Y., Yang, Z., Qiao, C., Liu, Y., Wang, C., Zeng, X., Hou, J., Huo, D., and Hou, C. (2024). Synergistic enhancement of wearable biosensor through Pt single-atom catalyst for sweat analysis. Biosens. Bioelectron. *258*, 116354. https://doi.org/10.1016/j.bios.2024.116354.
6. Wang, J., Wang, L., Li, G., Yan, D., Liu, C., Xu, T., and Zhang, X. (2022). Ultra-small wearable flexible biosensor for continuous sweat analysis. ACS Sens. *7*, 3102–3107. https://doi.org/10.1021/acssensors.2c01533.
7. Liu, K.K., Meng, Z., Fang, Y., and Jiang, H.L. (2023). Conductive MOFs for electrocatalysis and electrochemical sensor. eScience *3*, 100133. https://doi.org/10.1016/j.esci.2023.100133.
8. Zhang, S., Zhao, W., Zeng, J., He, Z., Wang, X., Zhu, Z., Hu, R., Liu, C., and Wang, Q. (2023). Wearable non-invasive glucose sensors based on metallic nanomaterials. Mater. Today. Bio *20*, 100638. https://doi.org/10.1016/j.mtbio.2023.100638.
9. Lee, H., Hong, Y.J., Baik, S., Hyeon, T., and Kim, D.H. (2018). Enzyme-based glucose sensor: from invasive to wearable device. Adv. Healthcare Mater. *7*, 1701150. https://doi.org/10.1002/adhm.201701150.
10. Moyer, J., Wilson, D., Finkelshtein, I., Wong, B., and Potts, R. (2012). Correlation between sweat glucose and blood glucose in subjects with diabetes. Diabetes Technol. Therapeut. *14*, 398–402. https://doi.org/10.1089/dia.2011.0262.
11. Tang, C., Zhou, K., Wang, R., Li, M., Liu, W., Li, C., Chen, X., Lu, Q., and Chang, Y. (2024). Wearable biosensors for human sweat glucose detection based on carbon black nanoparticles. Anal. Bioanal. Chem. *416*, 1407–1415. https://doi.org/10.1007/s00216-024-05135-w.

12. Hekmat, F., Ataei Kachouei, M., Taghaddosi Foshtomi, S., Shahrokhian, S., and Zhu, Z. (2023). Direct decoration of commercial cotton fabrics by binary nickel-cobalt metal-organic frameworks for flexible glucose sensing in next-generation wearable sensors. Talanta *257*, 124375. https://doi.org/10.1016/j.talanta.2023.124375.

13. Zhang, Q., Li, M., Wang, Z., Qin, C., Zhang, M., and Li, Y. (2020). Porous CuxO/Ag2O (x= 1, 2) nanowires anodized on nanoporous Cu-Ag bimetal network as a self-supported flexible electrode for glucose sensing. Appl. Surf. Sci. *515*, 146062. https://doi.org/10.1016/j.apsusc.2020.146062.

14. Wang, H., Liu, Z., Ding, J., Lepró, X., Fang, S., Jiang, N., Yuan, N., Wang, R., Yin, Q., Lv, W., et al. (2016). Downsized sheath–core conducting fibers for weavable superelastic wires, biosensors, supercapacitors, and strain sensors. Adv. Mater. *28*, 4998–5007. https://doi.org/10.1002/adma.201600405.

15. Zhu, C., Wu, J., Yan, J., and Liu, X. (2023). Advanced fiber materials for wearable electronics. Adv. Fiber Mater. *5*, 12–35. https://doi.org/10.1007/s42765-022-00212-0.

16. Zhu, X., Duan, M., Zhang, L., Zhao, J., Yang, S., Shen, R., Chen, S., Fan, L., and Liu, J. (2023). Liquid metal-enabled microspheres with high drug loading and multimodal imaging for artery embolization. Adv. Funct. Mater. *33*, 2209413. https://doi.org/10.1002/adfm.202209413.

17. Gao, Y., and Bando, Y. (2002). Carbon nanothermometer containing gallium. Nature *415*, 599. https://doi.org/10.1038/415599a.

18. Wang, R., Jiang, N., Su, J., Yin, Q., Zhang, Y., Liu, Z., Lin, H., Moura, F.A., Yuan, N., Roth, S., et al. (2017). A bi-sheath fiber sensor for giant tensile and torsional displacements. Adv. Funct. Mater. *27*, 1702134. https://doi.org/10.1002/adfm.201702134.

19. Daeneke, T., Khoshmanesh, K., Mahmood, N., de Castro, I.A., Esrafilzadeh, D., Barrow, S.J., Dickey, M.D., and Kalantar-Zadeh, K. (2018). Liquid metals: fundamentals and applications in chemistry. Chem. Soc. Rev. *47*, 4073–4111. https://doi.org/10.1039/C7CS00043J.

20. Akhter, R., and Maktedar, S.S. (2023). MXenes: Acomprehensive review of synthesis, properties, and progress in supercapacitor applications. Journal of Materiomics *9*, 1196–1241. https://doi.org/10.1016/j.jmat.2023.08.011.

21. Li, X., Shan, G., Ma, R., Shek, C.H., Zhao, H., and Ramakrishna, S. (2022). Bioinspired mineral MXene hydrogels for tensile strain sensing and radionuclide adsorption applications. Front. Physiol. *17*, 63501. https://doi.org/10.1007/s11467-022-1181-2.

22. Qin, R., Nong, J., Wang, K., Liu, Y., Zhou, S., Hu, M., Zhao, H., and Shan, G. (2024). Recent advances in flexible pressure sensors based on MXene materials. Adv. Mater. *36*, 2312761. https://doi.org/10.1002/adma.202312761.

23. Zhang, Y.Z., El-Demellawi, J.K., Jiang, Q., Ge, G., Liang, H., Lee, K., Dong, X., and Alshareef, H.N. (2020). MXene hydrogels: fundamentals and applications. Chem. Soc. Rev. *49*, 7229–7251. https://doi.org/10.1039/D0CS00022A.

24. Wang, Y., Qin, W., Yang, M., Tian, Z., Guo, W., Sun, J., Zhou, X., Fei, B., An, B., Sun, R., et al. (2023). High linearity, low hysteresis Ti3C2Tx MXene/AgNW/liquid metal self-healing strain sensor modulated by dynamic disulfide and hydrogen bonds. Adv. Funct. Mater. *33*, 2301587. https://doi.org/10.1002/adfm.202301587.

25. Jiang, S., Zhang, H., Li, Z., Chen, L., Yin, L., and Liu, X. (2023). Sponge-inspired MXene@ CeO2 detector for ultra-sensitive detection of glucose. Mater. Today Chem. *32*, 101638. https://doi.org/10.1016/j.mtchem.2023.101638.

26. Lin, P., Xie, J., He, Y., Lu, X., Li, W., Fang, J., Yan, S., Zhang, L., Sheng, X., and Chen, Y. (2020). MXene aerogel-based phase change materials toward solar energy conversion. Sol. Energy Mater. Sol. Cell. *206*, 110229. https://doi.org/10.1016/j.solmat.2019.110229.

27. Yang, J., Shen, M., Luo, Y., Wu, T., Chen, X., Wang, Y., and Xie, J. (2021). Advanced applications of chitosan-based hydrogels: From biosensors to intelligent food packaging system. Trends Food Sci. Technol. *110*, 822–832. https://doi.org/10.1016/j.tifs.2021.02.032.

28. Bark, H., and Lee, P.S. (2021). Surface modification of liquid metal as an effective approach for deformable electronics and energy devices. Chem. Sci. *12*, 2760–2777. https://doi.org/10.1039/D0SC05310D.

29. Zhao, Y., Zhao, K., Qian, R., Yu, Z., and Ye, C. (2024). Interfacial engineering of liquid metal nanoparticles for the fabrication of conductive hydrogels: A review. Chem. Eng. J. *486*, 150197. https://doi.org/10.1016/j.cej.2024.150197.

30. Babamiri, B., Sadri, R., Farrokhnia, M., Hassani, M., Kaur, M., Roberts, E.P.L., Ashani, M.M., and Sanati Nezhad, A. (2024). Molecularly Imprinted Polymer Biosensor Based on Nitrogen-Doped Electrochemically Exfoliated Graphene/Ti3 CNT X MXene Nanocomposite for Metabolites Detection. ACS Appl. Mater. Interfaces *16*, 27714–27727. https://doi.org/10.1021/acsami.4c01973.

31. Zhang, D., Cao, J., Zhang, X., Insin, N., Liu, R., and Qin, J. (2020). NiMn layered double hydroxide nanosheets in-situ anchored on Ti3C2 MXene via chemical bonds for superior supercapacitors. ACS Appl. Energy Mater. *3*, 5949–5964. https://doi.org/10.1021/acsaem.0c00863.

32. Lin, X., Song, D., Shao, T., Xue, T., Hu, W., Jiang, W., Zou, X., and Liu, N. (2024). A multifunctional biosensor via MXene assisted by conductive metal–organic framework for healthcare monitoring. Adv. Funct. Mater. *34*, 2311637. https://doi.org/10.1002/adfm.202311637.

33. Surdu-Bob, C.C., Saied, S.O., and Sullivan, J.L. (2001). An X-ray photoelectron spectroscopy study of the oxides of GaAs. Appl. Surf. Sci. *183*, 126–136. https://doi.org/10.1016/S0169-4332(01)00583-9.

34. Zhu, K., Shi, F., Zhu, X., and Yang, W. (2020). The roles of oxygen vacancies in electrocatalytic oxygen evolution reaction. Nano Energy *73*, 104761. https://doi.org/10.1016/j.nanoen.2020.104761.

35. Veerapandian, S., Jang, W., Seol, J.B., Wang, H., Kong, M., Thiyagarajan, K., Kwak, J., Park, G., Lee, G., Suh, W., et al. (2021). Hydrogen-doped viscoplastic liquid metal microparticles for stretchable printed metal lines. Nat. Mater. *20*, 533–540. https://doi.org/10.1038/s41563-020-00863-7.

36. Sun, B., Qiu, P., Liang, Z., Xue, Y., Zhang, X., Yang, L., Cui, H., and Tian, J. (2021). The fabrication of 1D/2D CdS nanorod@ Ti3C2 MXene composites for good photocatalytic activity of hydrogen generation and ammonia synthesis. Chem. Eng. J. *406*, 127177. https://doi.org/10.1016/j.cej.2020.127177.

37. Halim, J., Cook, K.M., Naguib, M., Eklund, P., Gogotsi, Y., Rosen, J., and Barsoum, M.W. (2016). X-ray photoelectron spectroscopy of select multilayered transition metal carbides (MXenes). Appl. Surf. Sci. *362*, 406–417. https://doi.org/10.1016/j.apsusc.2015.11.089.

38. Ahmad, R., and Lee, B.I. (2024). Facile fabrication of palm trunk–like ZnO hierarchical nanostructure–based biosensor for wide-range glucose detection. Chem. Eng. J. *492*, 152432. https://doi.org/10.1016/j.cej.2024.152432.

39. Wang, Q., Jiao, C., Wang, X., Wang, Y., Sun, K., Li, L., Fan, Y., and Hu, L. (2023). A hydrogel-based biosensor for stable detection of glucose. Biosens. Bioelectron. *221*, 114908. https://doi.org/10.1016/j.bios.2022.114908.

40. Kim, J.H., Kim, S., Dickey, M.D., So, J.H., and Koo, H.J. (2024). Interface of gallium-based liquid metals: oxide skin, wetting, and applications. Nanoscale Horiz. *9*, 1099–1119. https://doi.org/10.1039/D4NH00067F.

41. Okatenko, V., Castilla-Amorós, L., Stoian, D.C., Vávra, J., Loiudice, A., and Buonsanti, R. (2022). The native oxide skin of liquid metal Ga nanoparticles prevents their rapid coalescence during electrocatalysis. J. Am. Chem. Soc. *144*, 10053–10063. https://doi.org/10.1021/jacs.2c03698.

42. Lin, Y., Bariya, M., Nyein, H.Y.Y., Kivimäki, L., Uusitalo, S., Jansson, E., Ji, W., Yuan, Z., Happonen, T., Liedert, C., et al. (2019). Porous enzymatic membrane for nanotextured glucose sweat sensors with high stability toward reliable noninvasive health monitoring. Adv. Funct. Mater. *29*, 1902521. https://doi.org/10.1002/adfm.201902521.

43. Mirzajani, H., Abbasiasl, T., Mirlou, F., Istif, E., Bathaei, M.J., Dağ, Ç., Deyneli, O., Yazıcı, D., and Beker, L. (2022). An ultra-compact and wireless tag for battery-free sweat glucose monitoring. Biosens. Bioelectron. *213*, 114450. https://doi.org/10.1016/j.bios.2022.114450.

44. Li, M., Wang, L., Liu, R., Li, J., Zhang, Q., Shi, G., Li, Y., Hou, C., and Wang, H. (2021). A highly integrated sensing paper for wearable electrochemical sweat analysis. Biosens. Bioelectron. *174*, 112828. https://doi.org/10.1016/j.bios.2020.112828.

45. Zhang, H., Lin, F., Chen, G., Yang, C., Zhang, H., Yan, M., Li, H., Wang, X., Cheng, W., and Chen, Y. (2024). Intrinsically stretchable jellyfish-like gold nanowires film as multifunctional wearable chemical and physical sensors. Chem. Eng. J. *490*, 151798. https://doi.org/10.1016/j.jechem.2021.10.013.

STAR★METHODS

KEY RESOURCES TABLE

REAGENT or RESOURCE	SOURCE	IDENTIFIER
Chemicals, peptides, and recombinant proteins		
D (+)-Glucose	Adamas life	61055G
PBS (1×)	Adamas life	C8020
Chitosan	Adamas	89296GB
$FeCl_3$	Adamas	82296BD
Ethanol	Greagent	G73537AC
$Ti_3C_2T_x$ (5 mg/ml, etched)	Foshan Xinxi Technology Co., Ltd	N/A
Ga	Dongguan Dingguan Metal Technology Co., Ltd	N/A
Acetic acid	Shanghai Marel Biochemical Technology Co., Ltd	M22626
Artificial sweat (pH 6.5)	Shanghai Yuanye Biotechnology Co., Ltd	R26242
Other		
Scanning electron microscopy	ThermoFisher	Phenom Pure G6 Desktop SEM
X-ray photoelectron spectroscopy	ThermoFisher	ESCALAB 250Xi
X-ray diffractometer	Rigaku	MiniFlex600
USB flash drive electrochemical workstation	Shenzhen Refresh Biosensing Technology Co., Ltd	BioSYS-P15E Max
Flexible printed circuit board	Shenzhen Ruida Express Circuit Board Co., Ltd	N/A
Chip resistor (100Ω)	Nanjing Yincheng Zhichuang Electronic Technology Co., Ltd	N/A
Conductive silver paste	Shenzhen Jie Yongcheng Technology Co., Ltd	N/A
Conductive carbon paste	Shenzhen Jie Yongcheng Technology Co., Ltd	N/A

EXPERIMENTAL MODEL AND SUBJECT DETAILS

This study does not use experimental methods typical in the life sciences. Experiments were conducted using artificial sweat, which primarily consists of water, sodium chloride, urea, and lactic acid. To the artificial sweat, a specific concentration of glucose was added for testing the actual samples. The artificial sweat was procured from Shanghai Yuanye Biotechnology Co., Ltd.

METHOD DETAILS

Preparation of Ga@MXene/CS sensor

Firstly, chitosan was dissolved in dilute acetic acid and heated while stirring to form a chitosan hydrogel (Figure 1A). Subsequently, MXene dispersion was added to the chitosan hydrogel, and the mixture was subjected to continuous magnetic stirring for 30 minutes, yielding the MXene/CS hydrogel. Meanwhile, 0.6 g of Ga was ultrasonically dispersed in 5 mL of ethanol to prepare a Ga dispersion. This Ga dispersion was then introduced into the MXene/CS hydrogel, followed by magnetic stirring for 30 minutes to achieve uniform re-dispersion of Ga within the hydrogel, resulting in the Ga@MXene/CS composite. Finally, the Ga@MXene/CS composite was applied onto the working electrode area of the wearable sensor and dried at 40°C for 30 minutes.

Three-electrode system and sweat generator

The wearable sensor, illustrated in Figure 1B, is fabricated using a flexible printed circuit board (PCB) as the substrate. The flexible PCB includes five letters—S, I, M, I, and T—where "S", "M", and "T" serve as the working, reference, and counter electrodes of the detection system, respectively. The working electrode is coated with the prepared Ga@MXene/CS composite at the designated area. The reference electrode is made of Ag/AgCl.The fabrication process begins with coating the reference electrode area with silver paste, followed by drying at 120°C for 1 hour. The electrode is then immersed in a 0.5 M $FeCl_3$ solution for 1 minute, after which it is washed and dried to complete the preparation. The counter electrodes are prepared by applying carbon paste to the respective sections and drying for 1 hour.

The two letters "I" are used to construct the sweat-producing heater. In these regions, 100 Ω chip resistors are soldered to serve as heating elements. The sweat-producing heater operates using a constant voltage power supply, generating heat that induces

significant perspiration on the skin in contact with the sensor. As a result, the wearable sensor, which integrates a three-electrode system and a sweat-producing heater, enables real-time *in situ* detection.

Characterization

Scanning electron microscopy was employed to analyze the surface morphology and elemental composition of the electrodes. X-ray diffractometer was used to determine the crystalline phases of Ga/CS, MXene/CS, and MXene@Ga/CS. X-ray photoelectron spectroscopy was utilized to examine the elemental composition, chemical states, and molecular structure of the electrode modification layers. Electrochemical characterization and detection of the electrode modification layers were conducted using cyclic voltammetry (CV), electrochemical impedance spectroscopy (EIS), and differential pulse voltammetry (DPV) in a USB flash drive electrochemical workstation (Figure S6).

QUANTIFICATION AND STATISTICAL ANALYSIS

This study does not include statistical analysis or quantification.

ADDITIONAL RESOURCES

This study has not generated or contributed to a new website/forum and it is not part of a clinical trial.